

CoastSat: A Google Earth Engine-enabled Python toolkit to extract shorelines from publicly available satellite imagery

Kilian Vos^{*}, Kristen D. Splinter, Mitchell D. Harley, Joshua A. Simmons, Ian L. Turner

Water Research Laboratory, School of Civil and Environmental Engineering, UNSW Sydney, 110 King Street, Manly Vale, NSW, 2093, Australia

ARTICLE INFO

Keywords:

Google Earth Engine
Shoreline mapping
Landsat
Sentinel-2
Sub-pixel resolution

ABSTRACT

CoastSat is an open-source software toolkit written in Python that enables the user to obtain time-series of shoreline position at any sandy coastline worldwide from 30+ years (and growing) of publicly available satellite imagery. The toolkit exploits the capabilities of Google Earth Engine to efficiently retrieve Landsat and Sentinel-2 images cropped to any user-defined region of interest. The resulting images are pre-processed to remove cloudy pixels and enhance spatial resolution, before applying a robust and generic shoreline detection algorithm. This novel shoreline detection technique combines a supervised image classification and a sub-pixel resolution border segmentation to map the position of the shoreline with an accuracy of ~10 m. The purpose of *CoastSat* is to provide coastal managers, engineers and scientists a user-friendly and practical toolkit to monitor and explore their coastlines. The software is freely-available on GitHub (<https://github.com/kvos/CoastSat>) and is accompanied by guided examples (Jupyter Notebook) plus step-by-step README documentation.

Software availability

Software name: *CoastSat*

Developer: Kilian Vos

Year first official release: 2018

Hardware requirements: PC

System requirements: Windows, Linux, Mac

Program language: Python

Program size: 1 MB

Availability: <https://github.com/kvos/CoastSat>

License: GPL-3.0

Documentation: README in Github repository and guided example in the form of an editable Jupyter Notebook

1. Introduction

The coastal region is the most heavily urbanised land zone in the world (Small et al., 2011) and is regarded as a critical resource in view of its recreational, environmental and economic importance. Yet, ocean coasts are affected by variations in mean sea level, extreme waves, storm surges and river flow through a range of physical processes (Ranasinghe, 2016 for a review). Recent intensification in mean wave energy (Reguero et al., 2019), extreme coastal wave energy (Mentaschi et al., 2017)

and oceanic wind speeds (Young and Ribal, 2019), coupled with rising sea levels, suggest that coastal areas will be exposed to increasing hazards in coming decades (Li et al., 2018). It is therefore critical for coastal managers and policy makers regulating coastal development to observe and quantify these changes along coastlines vulnerable to extreme as well as subtle changes in oceanographic forcing (e.g., Barnard et al., 2017; Harley et al., 2017; Masselink et al., 2016). Data-scarcity, however, remains an ongoing challenge as long-term coastal monitoring programs, based on *in situ* measurements, are limited to only a few sites around the world (e.g., Barnard et al., 2015; Pianca et al., 2015; Turner et al., 2016). Indeed, shoreline data is key to understand past beach behaviour (Splinter et al., 2018) and calibrate numerical models capable of predicting future shoreline changes (Splinter et al., 2013). Publicly available remote sensing data from Earth Observation Satellites provides a low-cost solution to obtain long-term observations of coastline changes over the past three decades at many sites worldwide. Crucially, the advent of Google Earth Engine (Gorelick et al., 2017) has facilitated access to the growing archive of publicly available satellite imagery, providing the opportunity for global-scale analyses stretching back decades (e.g., Donchyts et al., 2016; Li et al., 2019; Luijendijk et al., 2018; Mentaschi et al., 2018).

Space-borne observations have been employed in a wide range of change detection applications, including the analysis of meandering

^{*} Corresponding author. Water Research Laboratory, School of Civil and Environmental Engineering, UNSW Sydney, Australia.

E-mail address: k.vos@unsw.edu.au (K. Vos).

<https://doi.org/10.1016/j.envsoft.2019.104528>

Received 6 February 2019; Received in revised form 11 June 2019; Accepted 24 September 2019

Available online 25 September 2019

1364-8152/© 2019 The Authors.

Published by Elsevier Ltd.

This is an open access article under the CC BY-NC-ND license

(<http://creativecommons.org/licenses/by-nc-nd/4.0/>).

river morphodynamics (Monegaglia et al., 2018), delineation of wetland footprints (Quinn and Epshtein, 2014) and identification of oil spills (Keramitsoglou et al., 2006). Recently, optical imaging satellites have begun to be used to measure the location of the shoreline (e.g., García-Rubio et al., 2015; Kuleli et al., 2011; Liu et al., 2017; Pardo-Pascual et al., 2012), which is regarded by coastal managers, planners, engineers and scientists as a key indicator of how coastlines vary and evolve over time. For instance, Hagenaaers et al. (2018) employed Landsat 5, Landsat 8 and Sentinel-2 image composites to map the position of the shoreline with a horizontal accuracy of the order of half a pixel (i.e., 15 m for Landsat images and 5 m for Sentinel-2 images), while Pardo-Pascual et al. (2018) evaluated a sub-pixel resolution shoreline detection technique at a low-energy microtidal beach and reported horizontal accuracies of less than 10 m using Landsat 7, Landsat 8 and Sentinel-2 images.

The aim of this short communication is to detail a new open-source software toolkit called *CoastSat* to obtain 30+ year time-series of approximately biweekly shoreline positions with a horizontal accuracy of ~ 10 m at any sandy coastline worldwide. Demonstrated in the accompanying Jupyter Notebook and README file is the suggested workflow to guide users to easily and efficiently: retrieve the required satellite imagery from the Google Earth Engine (GEE) archive of publicly available satellite imagery; apply a robust and generic sub-pixel resolution shoreline detection algorithm; and extract the required shoreline positions through time. Example practical applications of the *CoastSat* toolkit applied at contrasting sandy coastlines (tide range, wave climate) spanning Europe, the USA, Australia and New Zealand are presented in (Vos et al., 2019), where a range of storm, seasonal and inter-annual shorelines changes are illustrated.

2. Software capabilities

The toolkit is compatible with Python version 3.6 (or higher) and combines and extends the functionality of a number of other freely available Python software packages. The Google Earth Engine (GEE) Python API package is used to access the satellite imagery, while other machine learning and image processing packages, namely *scikit-learn* (Pedregosa et al., 2011) and *scikit-image* (van der Walt et al., 2014), are employed to automatically extract the position of the shoreline from the multispectral imagery. As is illustrated by a practical example provided in the accompanying Jupyter Notebook, the sequence of functionalities provided within the single *CoastSat* toolkit can be summarised as follows:

- (i) retrieval of the images from the GEE archive;
- (ii) pre-processing of the multispectral images (cloud masking, pansharping and down-sampling);
- (iii) sub-pixel resolution shoreline extraction; and
- (iv) time-series of shoreline position along shore-normal transects.

CoastSat outputs the mapped shorelines as a .geojson file that can be imported into a GIS application. A flow chart of the different steps involved to obtain satellite-derived shorelines at a user-defined site is summarised in Fig. 1, and now described in further detail below.

2.1. Access to publicly available satellite imagery

The *Coastsat* toolkit provides an interface to the GEE API to enable easy access to all the TOA (Top-of-Atmosphere) reflectance images from the Landsat 5 (TM), Landsat 7 (ETM+) and Landsat 8 (OLI) Tier 1 collections as well as Sentinel-2 (MSI) Level-1C products, which also represent TOA reflectance. TOA images are calibrated to provide a

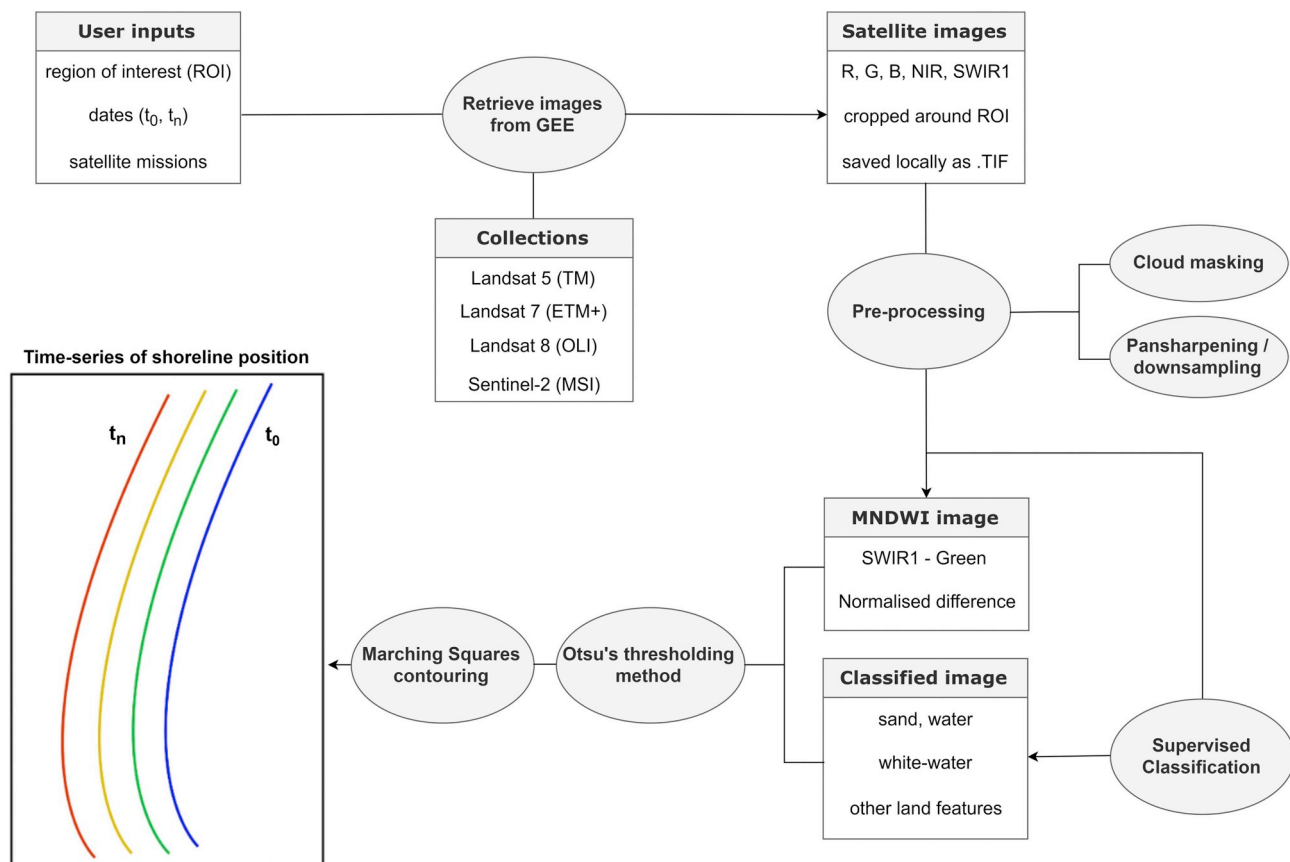


Fig. 1. Flow chart outlining the functionalities of *CoastSat*. Time-series of shoreline position are obtained over any user-defined region of interest and date range.

standardised comparison between images acquired by different sensors on different dates (Chander et al., 2009), thus they are suitable for time-series analysis. The user can choose which satellite mission(s) to use and all four missions can be used at the same time to maximise temporal resolution. To significantly reduce the size of the individual files (from several GBs to less than a MB per 5 km² region), a user-defined region of interest (ROI) is used to crop the images while still on the GEE server and prior download. In addition, only the spectral bands that are required for the shoreline detection, namely the three visible bands (R, G, B), the near infrared band (NIR) and the short-wave infrared band (SWIR1) are included in the downloaded cropped image. This implementation significantly increases processing speed and reduces memory usage on the local computer. For example, 30+ years of biweekly images of a 5 km² ROI can be downloaded and processed in ~2 h on a standard laptop (4 GB RAM, Intel Core i5), without running into memory allocation problems. Users should avoid requesting very large ROIs (>100 km²) as this will significantly slow down the processing, instead multiple smaller ROIs should be requested. Table 1 summarises the satellite data retrieved by *CoastSat*, including the GEE collections in which the images are continuously stored and the time coverage, revisit period, and pixel size of each satellite mission.

2.2. Pre-processing

Prior to extracting the shoreline, the TOA images are pre-processed as follows:

Cloud masking: each image is supplemented by a Quality Assessment band, pre-computed by the data provider (USGS for Landsat or ESA for Sentinel-2), which contains a per-pixel cloud mask. With this information, the percentage of cloud cover is calculated based on the number of cloudy pixels inside the region of interest and a user-defined cloud cover threshold is used to discard all the images that exceed a certain percentage of cloud cover.

Panchromatic image sharpening and down-sampling: in this next pre-processing step the spatial resolution of the satellite image is enhanced to achieve an optimal shoreline detection. For Landsat 7 (ETM+) and Landsat 8 (OLI) images, the higher resolution panchromatic band (see Table 1) is used to increase the resolution of the bands, whose portion of the electromagnetic spectrum is covered by the panchromatic band, from 30 to 15 m by applying a data fusion method based on principal component analysis (Tu et al., 2001). In this method, the multispectral bands are down-sampled to 15 m (by bilinear interpolation) and decomposed in principal components, then the first principal component is replaced by the panchromatic band (after matching the histograms) and retransformed back into the original multispectral space. Landsat 5 (TM) images do not have a panchromatic band,

Table 1

Summary of the different datasets of satellite imagery that can be accessed with *CoastSat*.

| Satellite mission | GEE collection | Time coverage | Revisit period | Pixel size |
|-------------------|----------------------------|---------------|----------------|---|
| Landsat 5 (TM) | LANDSAT/LT05/C01/T1_TOA | 1984–2013 | 16 days | 30 m R, G, B, NIR, SWIR1 bands |
| Landsat 7 (ETM+) | LANDSAT/LE07/C01/T1_RT_TOA | 1999–present | 16 days | 30 m R, G, B, NIR, SWIR1 bands + 15 m panchromatic band |
| Landsat 8 (OLI) | LANDSAT/LC08/C01/T1_RT_TOA | 2013–present | 16 days | 30 m R, G, B, NIR, SWIR1 bands + 15 m panchromatic band |
| Sentinel-2 (MSI) | COPERNICUS/S2 | 2015–present | 5 days | 10 m R, G, B, NIR + 20 m SWIR1 |

however the 30 m bands are down-sampled to 15 m by bilinear interpolation as this was found to improve the accuracy of the shoreline detection. For Sentinel-2 images, the 20 m SWIR1 band is down-sampled to 10 m by bilinear interpolation, so that all the bands are at 10 m resolution.

It should be noted that the images are orthorectified by the data provider and no further geometric correction (i.e. co-registration) is applied in *CoastSat*. The georeferencing accuracy of each image is stored in the output file containing the mapped shorelines.

2.3. Shoreline detection

The shoreline is defined here as the instantaneous interface between water and sand captured at the instant of image acquisition. The *CoastSat* toolkit applies a robust sub-pixel resolution shoreline detection algorithm to the pre-processed satellite images. The algorithm builds upon the sub-pixel border segmentation by Liu et al. (2017), as was originally proposed by Cipolletti et al. (2012). As a further refinement of these techniques, the method that is implemented within *CoastSat* introduces a new image classification component that refines the shoreline detection. There are two core steps in this algorithm: (i) image classification into four classes; (ii) sub-pixel resolution border segmentation. These steps are further described below. Furthermore, before running the batch shoreline detection on all the downloaded images the user has the option to manually digitise the position of a ‘reference shoreline’ that approximates this sand/water interface on one of the cloud-free images. The coordinates of this shoreline provide a reference for the subsequent automatically detected shorelines and assist to exclude outliers and false detections.

2.3.1. Image classification

A Neural Network classifier (Civco, 1993), referred to as Multilayer Perceptron in *scikit-learn*, is used to label each pixel of the image with one of four classes: ‘sand’, ‘water’, ‘white-water’, ‘other land features’ (e.g., vegetation, buildings, rocky headlands). A set of 20 features (i.e., explanatory variables) are used as inputs for the classifier, these include the pixel intensity in 5 multispectral bands (i.e., R, G, B, NIR, SWIR1), 5 commonly used spectral indices (e.g., water index, vegetation index etc ...) and the variance (calculated using a 3 × 3 moving window) of each multispectral band and spectral index. The image variance proved to be very efficient at discriminating ‘sand’ pixels, which have a low variance as the neighbouring pixels are also ‘sand’, from rooftops and other isolated bright objects which tend to have a higher variance as they are surrounded by darker pixels (e.g., roads and trees). The classifier was trained beforehand (the user does not have to train it) with a set of 5,000 pixels in each class, manually digitised from 50 satellite images covering 5 different sites (training data available in Vos, 2019). A 10-fold cross-validation was performed to test the accuracy of the classifier, resulting in 99% of the pixels being correctly classified. Fig. 2 includes an example Sentinel-2 (MSI) satellite image (Fig. 2a) and the corresponding classified image (Fig. 2b). Additionally, if the user’s site of interest is made of dark sand, a second classifier specifically trained on black/grey sand beaches is available in the toolbox.

2.3.2. Sub-pixel resolution border segmentation

In this second step of shoreline detection, the boundary between sand and water is extracted using the Modified Normalized Difference Water Index (MNDWI) applied to each of the classified images (Section 2.3.1). The MNDWI (Xu, 2006) is calculated as follows:

$$MNDWI = \frac{SWIR1 - G}{SWIR1 + G} \quad (1)$$

where *SWIR1* and *G* are the pixel intensity in the short-wave infrared band and green band, respectively. The MNDWI values range between −1 and 1 as shown in Fig. 2c. Next, a histogram of MNDWI values is

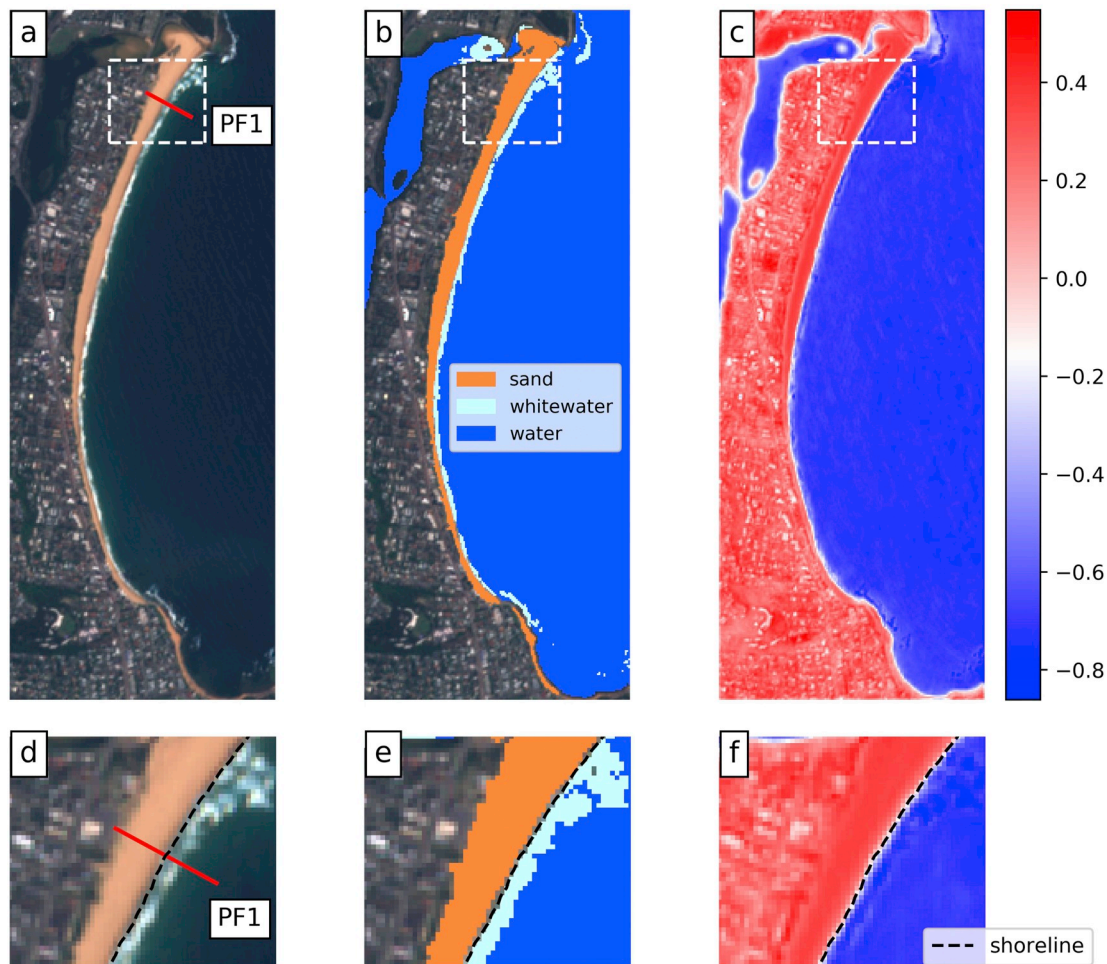


Fig. 2. a) Example region of interest within RGB image located at Narrabeen-Collaroy in southeast Australia, Sentinel-2 (MSI). b) Output of image classification where each pixel has been labelled with one of three classes: 'sand', 'white-water' and 'water' (the 4th class 'other land features' corresponds to the unlabelled pixels). c) Grayscale (i.e. single colour band) image of the MNDWI pixel values. d), e) and f) Insets showing the detected shoreline, respectively on the RGB image, classified image and MNDWI image.

constructed with the labelled pixels located within a pre-defined distance (nominally set to 150 m in the toolkit) from 'sand' pixels as illustrated in Fig. 3. In the resulting histogram, the probability density function (PDF) of the 'sand' pixels is centred around positive values of MNDWI, while the 'water' pixels have negative MNDWI values. Accordingly, the 'sand'/'water' threshold is computed applying Otsu's thresholding algorithm (Otsu, 1979) to find the MNDWI value that maximises inter-class variance between the 'sand' and 'water' distributions, excluding upfront the pixels belonging to the 'white-water' and 'other land features' class. The presence of 'white-water' is known to

cause errors in the shoreline detection: Hagenaaers et al. (2018) report seaward offsets of up to 40 m in the presence of wave-induced foam; and Pardo-Pascual et al. (2018) notes white-water as being one of the largest sources of error. Indeed, the histogram of MNDWI values in Fig. 3 reveals that the pixels belonging to the 'white-water' class span a broad range of values with no distinct peak and therefore do not assist in discriminating the shoreline and may in fact lead to false detections.

The final step in the detection of individual shorelines is to compute the iso-valued contour on the MNDWI image for a level equal to the 'sand'/'water' threshold. This operation is done at sub-pixel resolution

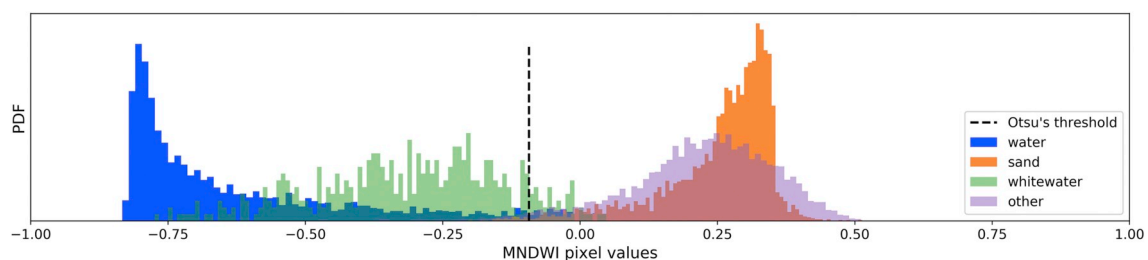


Fig. 3. Histogram computed from the same region of interest shown in Fig. 2, showing the probability density function (PDF) of MNDWI values for each of the four labelled classes ('water', 'sand', 'whitewater' and 'other land features'). Otsu's threshold (Otsu, 1979) is computed as the threshold that maximises inter-class variance between the 'sand' and 'water' classes, ignoring the 'white-water' and 'other land features' classes which do not contribute to identify the shoreline (i. e., sand/water interface).

by applying the Marching Squares algorithm (Cipolletti et al., 2012; Lorensen and Cline, 1987). This iso-valued contour represents the shoreline (Fig. 2d, 2e and 2f) and matches with the sand/water interface.

2.4. Post-processing

CoastSat outputs for the user each mapped shoreline as a vector of 2D coordinates in a user-defined spatial reference system, associated with the exact acquisition date and time in Coordinated Universal Time (UTC). For quality control, *CoastSat* offers the option to visualise and accept/reject each detected shoreline by the application of an interactive graphical tool.

Once the shorelines have been extracted, the *Coastsat* toolkit offers the option to intersect the 2D shorelines with shore-normal transects and extract time-series of cross-shore shoreline change along those transects. The user can either manually digitise the transects with an *ad hoc* interactive tool or import the transect coordinates from a separate file. To minimise the effect of localised water levels due to wave runup on the beach face (i.e., swash), the intersection between the instantaneous shoreline and the shore-normal transects is calculated as the alongshore average of the shoreline points located within 25 m (default value which can be modified by the user) of the transect.

It is recommended that along coastlines with large tide ranges and/or flatter beach profiles, all shorelines be adjusted to a standard reference elevation. Since every image is acquired at a different stage of the tide, a linear tidal correction can be applied using measured water levels and characteristic beach face slope to translate each shoreline to a reference elevation as follows:

$$\Delta x = \frac{z_{\text{ref}} - z_{\text{wl}}}{m} \quad (2)$$

where Δx is the cross-shore horizontal shift along the shore-normal transects, z_{ref} is the reference elevation (e.g., 0 m above mean sea level), z_{wl} is the local water level (tide + residuals) at the time of image acquisition, and m is a characteristic beach face slope. The precise time of image acquisition to obtain the local water level is stored in the image metadata. For sites where measurements of local water levels and beach slope may not be available, practical guidance on tidal correction is provided in Section 3.3. Note that the tidal correction is not implemented in the toolbox as it is site-specific.

3. Results and discussion

3.1. Validation example

This short communication describes the use of the *CoastSat* software package to extract shorelines using GEE images at any user-defined coastline location and region of interest around the world. For illustration, the accuracy of the resulting satellite-derived shoreline time-series is compared here to in-situ field measurements that have been obtained since the mid 1970's at a survey transect located toward the north end of the Narrabeen-Collaroy embayment in southeast Australia and labelled as 'Profile 1' (PF1) in Fig. 2a.

Narrabeen-Collaroy is a world-renowned coastal monitoring site situated on the Northern Beaches of Sydney. The 3.6 km long embayment has been surveyed monthly since 1976 at five cross-shore transects and the uninterrupted dataset is publicly available and described in Turner et al. (2016). The tidal regime is microtidal (mean spring tide range 1.3 m) and the characteristic beach face slope is 0.1.

All suitable and publicly available satellite images covering Narrabeen-Collaroy were retrieved and processed using *CoastSat* as described in Section 2. A total of 502 satellite-derived shorelines were extracted between 1987 and 2018. A time-series of shoreline cross-shore position was obtained by computing the intersection between the extracted shorelines and the shore-normal transect PF1 (see Fig. 2d).

Post-processing of the shoreline data was undertaken to translate all data to $z_{\text{ref}} = 0.7$ m relative to the Australian Height Datum (corresponding to Mean High Water Springs at Narrabeen).

Fig. 4 compares the time-series of cross-shore position obtained from in-situ field measurements and satellite-derived shorelines at this location. The satellite-derived shorelines match very well with the in-situ observations, with a coefficient of determination of 0.8, a RMSE of 7.2 m, a slight seaward bias of 1.4 m and 90% of the errors falling within 11.2 m. The single validation example presented here for the purpose of illustration, is representative of larger and more comprehensive analyses presented in Vos et al. (2019), where satellite-derived shorelines were compared against long-term in-situ shoreline measurements at 5 diverse sites: the observed horizontal accuracies (RMSE) varied between 7.3 m at a microtidal beach with a steep beach face slope and 12.7 m at a mesotidal beach with a gentle slope.

3.2. Comparison to previous methods

The time-series validation example presented above shows that satellite-derived shorelines from *CoastSat* capture major erosion events (e.g., 60 m of shoreline recession in June 2016), as well as seasonal to interannual behaviour. The methodology is also capable of capturing the effects of engineering interventions and beach rotation (see example applications in Vos et al. (2019)). This result indicates that the enhancement of the image resolution (Section 2.2) and application of a sub-pixel resolution technique (Section 2.3.2) makes it possible to map individual shorelines with sub-pixel accuracy (i.e., smaller than the pixel resolution of 10 m for Sentinel-2 and 30 m for Landsat). The sub-pixel methodology ensures no significant variability in the accuracy of the final satellite-derived shoreline despite changing resolution of the satellites (see Table 1).

In contrast to previous toolboxes using satellite data (Monegaglia et al., 2018; Montzka et al., 2008; Quan et al., 2017), the *CoastSat* toolkit leverages the GEE software so that the user can simply and efficiently retrieve hundreds of multispectral images, cropped around any user-defined region of interest, using a standard desktop computer. This enables the user to bypass the time-consuming task of manually downloading large satellite images from the USGS Earth Explorer (or other web portals), which are provided as large files of several GBs and may contain irrelevant data (i.e., areas outside the region of interest, thermal bands, etc).

CoastSat uses a newly developed generic and robust automated shoreline detection algorithm that integrates an image classification component into a sub-pixel resolution border segmentation of the MNDWI. Compared to previous studies that map the shoreline by applying a thresholding algorithm to the entire image (e.g., Hagenaars et al., 2018; Kuleli et al., 2011; Liu et al., 2017), this new method uses a four-class classification to specifically extract the boundary between pre-classified water and sand pixels only, removing from this critical process all other pixels corresponding to vegetation, buildings, roads, white-water, rocky headlands, etc. This improvement refines the shoreline detection methodology, as previous studies that derived satellite shorelines at Narrabeen-Collaroy have reported lower accuracies for the same dataset; for example, the recent work by Luijendijk et al. (2018), in which the Narrabeen dataset was also used as one of four validation cases, reports an RMSE of 13.7 m at this same location. Additionally, this improved approach to shoreline detection can be more readily applied to different coastal settings, since the algorithm is indifferent to the presence of urban areas, forests or large amounts of white-water in the image, that are effectively excluded from the analyses by the new 4-class classification.

3.3. Practical guidance on tidal correction

The satellites of the Landsat and Sentinel-2 constellations are launched into sun-synchronous orbits, which ensure that the angle of

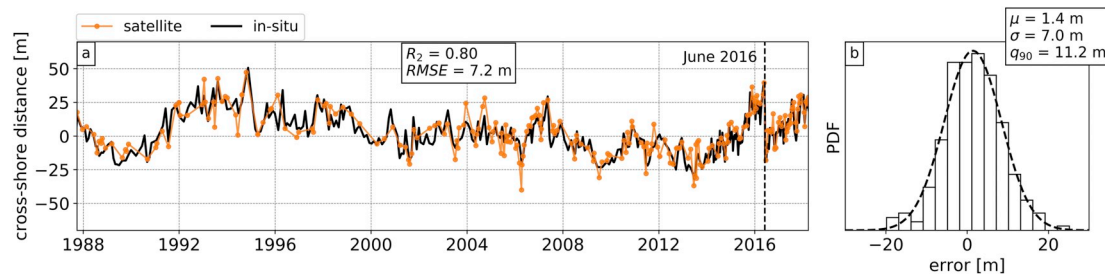


Fig. 4. a) Tidally-corrected time-series of shoreline position extracted by CoastSat along transect PF1 at Narrabeen-Collaroy, Australia. b) Histogram of the horizontal errors, the dashed line indicates a fitted normal distribution.

sunlight upon the Earth's surface is constant for all image acquisitions. To achieve this, all Landsat and Sentinel-2 images are acquired between 10 and 10:30 a.m. local time, at constant revisit periods of respectively 16 and 5 days. Consequently, only fixed combinations of the diurnal/semi-diurnal and neap-spring tidal cycles are sampled by the sun-synchronous sensors, which may result in tidal aliasing (Bishop-Taylor et al., 2019; Eleveld et al., 2014). Thus, the time-series of shoreline change along shore-normal transects extracted with *CoastSat* may contain a tidal bias that the user should be aware of. For instance, the non-tidally corrected time-series along PF1 at Narrabeen result in a 7.2 m mean error, compared to a 1.4 m mean error for the tidally-corrected time-series shown in Fig. 4.

When applying the tidal correction with Equation (2), users should employ the best water level and slope data that is available to them. The UNESCO Sea Level Station Monitoring Facility (VLIZ, 2018) and Global Sea Level Observing System (PSMSL, 2019) provide data from a global network of tide gauges. In the absence of a local tide gauge, predicted tides can be obtained at any location in the world from global tide models such as FES2014 (Carrere et al., 2016). The predicted tides do not capture tidal anomalies, but they will minimise any potential bias in the time-series caused by tidal aliasing. A representative intertidal beach slope can be obtained from a GPS survey or LIDAR flight of the area. At Narrabeen PF1, it was found that no significant improvement in the error statistics was obtained when using a time-varying beach slope (based on biweekly transect surveys) instead of an average beach slope.

4. Conclusions

The growing database of 30+ years of satellite images freely available via Google Earth Engine (GEE) constitutes the longest, continuously running monitoring of coastlines around the world. This short communication describes and illustrates an open-source Python toolkit that enables the user to obtain time-series of shoreline position at any coastline worldwide from 30+ years (and growing) of publicly available satellite imagery. The software is easy to use, freely available and open-source. Importantly, the ability to observe and quantify shoreline changes over the past three decades is key to present-day coastal management and *CoastSat* represents a valuable tool for a range of potential users including (but not limited to):

- policy makers responsible for regulating coastal development;
- coastal managers and engineers designing and implementing coastal protection;
- researchers evaluating the impacts of climate change and oceanographic forcing within the coastal zone.

Finally, increasing population pressure on ocean coasts and climate change driven variations in storminess patterns (frequency and intensity), wave climate and water levels, strongly suggest the need to plan for future adaptation of the coastal community (Mills et al., 2018). However, successful future coastal planning relies on an improved understanding of the links between spatial patterns of coastal change and

environmental forcings regulated by climate drivers (Barnard et al., 2015). In this context, *CoastSat* offers the capability to monitor coastline changes globally at short (seasonal) and long (decadal) time scales using satellite remote sensing to provide vital understanding of the relationship between climate drivers and coastline response into the future.

Acknowledgments

The authors wish to acknowledge the efforts of the United States Geological Survey and the European Space Agency in providing high-quality open-access data to the scientific community and Google Earth Engine for facilitating the access to the archive of publicly available satellite imagery. The authors are particularly grateful to Sean Vitousek and two anonymous reviewers for their insightful comments and suggestions that greatly improved the manuscript. The authors would also like to thank Chris Leaman for helping to improve the *CoastSat* toolbox. Funding for the routine monitoring at Narrabeen is generously provided by Northern Beaches Council (formerly Warringah Council), UNSW Research Infrastructure Scheme, UNSW Faculty of Engineering Early Career Grant, the NSW Adaptation Research Hub – Coastal Processes Node (Office of Environment and Heritage), and the Australian Research Council (LP0455157, LP100200348, DP150101339, LP170100161). Manly Hydraulics Laboratory provided tide data on behalf of the NSW Office of Environment and Heritage. The first author is supported by the UNSW Scientia PhD Scholarship Scheme.

Appendix A. Supplementary data

Supplementary data to this article can be found online at <https://doi.org/10.1016/j.envsoft.2019.104528>.

References

- Barnard, P.L., Hoover, D., Hubbard, D.M., Snyder, A., Ludka, B.C., Allan, J., Kaminsky, G.M., Ruggiero, P., Gallien, T.W., Gabel, L., McCandless, D., Weiner, H.M., Cohn, N., Anderson, D.L., Serafin, K.A., 2017. Extreme oceanographic forcing and coastal response due to the 2015–2016 El Niño. *Nat. Commun.* 8. <https://doi.org/10.1038/ncomms14365>.
- Barnard, P.L., Short, A.D., Harley, M.D., Splinter, K.D., Vitousek, S., Turner, I.L., Allan, J., Banno, M., Bryan, K.R., Doria, A., Hansen, J.E., Kato, S., Kuriyama, Y., Randall-Goodwin, E., Ruggiero, P., Walker, I.J., Heathfield, D.K., 2015. Coastal vulnerability across the Pacific dominated by El Niño/Southern oscillation. *Nat. Geosci.* 8, 801–807. <https://doi.org/10.1038/ngeo2539>.
- Bishop-Taylor, R., Sagar, S., Lymburner, L., Beaman, R.J., 2019. Between the tides: modelling the elevation of Australia's exposed intertidal zone at continental scale. *Estuar. Coast Shelf Sci.* 223, 115–128. <https://doi.org/10.1016/j.ecss.2019.03.006>.
- Carrere, L., Lyard, F., Cancet, M., Guillot, A., Picot, N., 2016. FES 2014, a new tidal model—validation results and perspectives for improvements. In: *Proceedings of the ESA Living Planet Symposium*, pp. 9–13.
- Chander, G., Markham, B.L., Helder, D.L., 2009. Summary of current radiometric calibration coefficients for Landsat MSS, TM, ETM+, and EO-1 ALI sensors. *Remote Sens. Environ.* 113, 893–903. <https://doi.org/10.1016/j.rse.2009.01.007>.
- Cipolletti, M.P., Delrieux, C.A., Perillo, G.M.E., Cintia Piccolo, M., 2012. Superresolution border segmentation and measurement in remote sensing images. *Comput. Geosci.* 40, 87–96. <https://doi.org/10.1016/j.cageo.2011.07.015>.
- Civco, D.L., 1993. Artificial neural networks for land-cover classification and mapping. *Int. J. Geogr. Inf. Syst.* 7, 173–186. <https://doi.org/10.1080/02693799308901949>.

- Donchyts, G., Baart, F., Winsemius, H., Gorelick, N., Kwadijk, J., Van De Giesen, N., 2016. Earth's surface water change over the past 30 years. *Nat. Clim. Chang.* 6, 810–813. <https://doi.org/10.1038/nclimate3111>.
- Eleveld, M.A., Van der Wal, D., Van Kessel, T., 2014. Estuarine suspended particulate matter concentrations from sun-synchronous satellite remote sensing: tidal and meteorological effects and biases. *Remote Sens. Environ.* 143, 204–215. <https://doi.org/10.1016/j.rse.2013.12.019>.
- García-Rubio, G., Huntley, D., Russell, P., 2015. Evaluating shoreline identification using optical satellite images. *Mar. Geol.* 359, 96–105. <https://doi.org/10.1016/j.margeo.2014.11.002>.
- Gorelick, N., Hancher, M., Dixon, M., Ilyushchenko, S., Thau, D., Moore, R., 2017. Google Earth engine: planetary-scale geospatial analysis for everyone. *Remote Sens. Environ.* 202, 18–27. <https://doi.org/10.1016/j.rse.2017.06.031>.
- Hagenaars, G., de Vries, S., Luijendijk, A.P., de Boer, W.P., Reniers, A.J.H.M., 2018. On the accuracy of automated shoreline detection derived from satellite imagery: a case study of the sand motor mega-scale nourishment. *Coast. Eng.* 133, 113–125. <https://doi.org/10.1016/j.coastaleng.2017.12.011>.
- Harley, M.D., Turner, I.L., Kinsela, M.A., Middleton, J.H., Mumford, P.J., Splinter, K.D., Phillips, M.S., Simmons, J.A., Hanslow, D.J., Short, A.D., 2017. Extreme coastal erosion enhanced by anomalous extratropical storm wave direction. *Sci. Rep.* 7, 6033. <https://doi.org/10.1038/s41598-017-05792-1>.
- Keramitsoglou, I., Cartalis, C., Kiranoudis, C.T., 2006. Automatic identification of oil spills on satellite images. *Environ. Model. Softw.* 21, 640–652. <https://doi.org/10.1016/j.envsoft.2004.11.010>.
- Kuleli, T., Guneroglu, A., Karsli, F., Dihkan, M., 2011. Automatic detection of shoreline change on coastal Ramsar wetlands of Turkey. *Ocean Eng.* 38, 1141–1149. <https://doi.org/10.1016/j.oceaneng.2011.05.006>.
- Li, H., Wan, W., Fang, Y., Zhu, S., Chen, X., Liu, B., Yang, H., 2019. A Google Earth engine-enabled software for efficiently generating high-quality user-ready landsat mosaic images. *Environ. Model. Softw.* 112, 16–22. <https://doi.org/10.1016/j.envsoft.2018.11.004>.
- Li, N., Yamazaki, Y., Roeder, V., Cheung, K.F., Chock, G., 2018. Probabilistic mapping of storm-induced coastal inundation for climate change adaptation. *Coast. Eng.* 133, 126–141. <https://doi.org/10.1016/j.coastaleng.2017.12.013>.
- Liu, Q., Trinder, J., Turner, I.L., 2017. Automatic super-resolution shoreline change monitoring using Landsat archival data: a case study at Narrabeen–Collaroy Beach, Australia. *J. Appl. Remote Sens.* 11, 016036. <https://doi.org/10.1117/1.JRS.11.016036>.
- Lorensen, W.E., Cline, H.E., 1987. Marching cubes: a high resolution 3D surface construction algorithm. In: *Proceedings of the 14th Annual Conference on Computer Graphics and Interactive Techniques - SIGGRAPH '87*, pp. 163–169. <https://doi.org/10.1145/37401.37422>.
- Luijendijk, A., Hagenaars, G., Ranasinghe, R., Baart, F., Donchyts, G., Aarninkhof, S., 2018. The state of the world's beaches. *Sci. Rep.* 1–11. <https://doi.org/10.1038/s41598-018-24630-6>.
- Masselink, G., Castelle, B., Scott, T., Dodet, G., Suanez, S., Jackson, D., Floe, F., 2016. Extreme wave activity during 2013/2014 winter and morphological impacts along the Atlantic coast of Europe. *Geophys. Res. Lett.* 2135–2143. <https://doi.org/10.1002/2015GL067492>.
- Mentaschi, L., Voudoukas, M.I., Pekel, J.-F., Voukouvalas, E., Feyen, L., 2018. Global long-term observations of coastal erosion and accretion. *Sci. Rep.* 8, 12876. <https://doi.org/10.1038/s41598-018-30904-w>.
- Mentaschi, L., Voudoukas, M.I., Voukouvalas, E., Dosio, A., Feyen, L., 2017. Global changes of extreme coastal wave energy fluxes triggered by intensified teleconnection patterns. *Geophys. Res. Lett.* 44, 2416–2426. <https://doi.org/10.1002/2016GL072488>.
- Mills, A.K., Bolte, J.P., Ruggiero, P., Serafin, K.A., Lipiec, E., Corcoran, P., Stevenson, J., Zanolto, C., Lach, D., 2018. Exploring the impacts of climate and policy changes on coastal community resilience: simulating alternative future scenarios. *Environ. Model. Softw.* 109, 80–92. <https://doi.org/10.1016/j.envsoft.2018.07.022>.
- Monegaglia, F., Zolezzi, G., Güneralp, I., Henshaw, A.J., Tubino, M., 2018. Automated extraction of meandering river morphodynamics from multitemporal remotely sensed data. *Environ. Model. Softw.* 105, 171–186. <https://doi.org/10.1016/j.envsoft.2018.03.028>.
- Montzka, C., Canty, M., Kreins, P., Kunkel, R., Menz, G., Vereecken, H., Wendland, F., 2008. Multispectral remotely sensed data in modelling the annual variability of nitrate concentrations in the leachate. *Environ. Model. Softw.* 23, 1070–1081. <https://doi.org/10.1016/j.envsoft.2007.11.010>.
- Otsu, N., 1979. A threshold selection method from gray-level histograms. *IEEE Trans. Syst. Man Cybern.* 20, 62–66. <https://doi.org/10.1109/tsmc.1979.4310076>.
- Pardo-Pascual, J.E., Almonacid-Caballer, J., Ruiz, L.A., Palomar-Vázquez, J., 2012. Automatic extraction of shorelines from Landsat TM and ETM+ multi-temporal images with subpixel precision. *Remote Sens. Environ.* 123, 1–11. <https://doi.org/10.1016/j.rse.2012.02.024>.
- Pardo-Pascual, J.E., Sánchez-García, E., Almonacid-Caballer, J., Palomar-Vázquez, J.M., de los Santos, E.P., Fernández-Sarria, A., Balaguer-Beser, A., 2018. Assessing the accuracy of automatically extracted shorelines on microtidal beaches from landsat 7, landsat 8 and sentinel-2 imagery. *Remote Sens.* 10. <https://doi.org/10.3390/rs10020326>.
- Pedregosa, F., Varoquaux, G., Gramfort, A., Michel, V., Thirion, B., Grisel, O., Blondel, M., Prettenhofer, P., Weiss, R., Dubourg, V., Vanderplas, J., Passos, A., Cournapeau, D., Brucher, M., Perrot, M., Duchesnay, É., 2011. Scikit-learn machine learning in Python. *J. Mach. Learn. Res.* 12, 2825–2830. <https://doi.org/10.1007/s13398-014-0173-2>.
- Pianca, C., Holman, R.A., Siegle, E., 2015. Shoreline variability from days to decades: results of long-term video imaging. *J. Geophys. Res. Ocean.* 1–17. <https://doi.org/10.1002/2014JC010320>.
- PSMSL, 2019. Global Sea level observing system (GLOSS) [WWW Document]. <https://www.psmsl.org/gloss/>. accessed 5.14.19.
- Quan, X., He, B., Yebra, M., Yin, C., Liao, Z., Li, X., 2017. Retrieval of forest fuel moisture content using a coupled radiative transfer model. *Environ. Model. Softw.* 95, 290–302. <https://doi.org/10.1016/j.envsoft.2017.06.006>.
- Quinn, N.W.T., Epshteyn, O., 2014. Seasonally-managed wetland footprint delineation using landsat ETM+ satellite imagery. *Environ. Model. Softw.* 54, 9–23. <https://doi.org/10.1016/j.envsoft.2013.12.012>.
- Ranasinghe, R., 2016. Assessing climate change impacts on open sandy coasts: a review. *Earth Sci. Rev.* <https://doi.org/10.1016/j.earscirev.2016.07.011>.
- Reguero, B.G., Losada, I.J., Méndez, F.J., 2019. A recent increase in global wave power as a consequence of oceanic warming. *Nat. Commun.* 10, 1–14. <https://doi.org/10.1038/s41467-018-08066-0>.
- Small, C., Nicholls, R.J., Summer, F., Small, C., 2011. A global analysis of human settlement in coastal zones. *J. Coast. Res.* 19, 584–599. <https://doi.org/10.2307/4299200>.
- Splinter, K.D., Harley, M.D., Turner, I.L., 2018. Remote sensing is changing our view of the coast: insights from 40 years of monitoring at Narrabeen–Collaroy, Australia. *Remote Sens.* 10. <https://doi.org/10.3390/rs1011744>.
- Splinter, K.D., Turner, I.L., Davidson, M.A., 2013. How much data is enough? The importance of morphological sampling interval and duration for calibration of empirical shoreline models. *Coast. Eng.* 77, 14–27. <https://doi.org/10.1016/j.coastaleng.2013.02.009>.
- Tu, T.-M., Su, Shu-C., Shyu, H., Huang, P.S., 2001. A new look at IHS-like image fusion methods. *Inf. Fusion* 2, 177–186. [https://doi.org/10.1016/S1566-2535\(01\)00036-7](https://doi.org/10.1016/S1566-2535(01)00036-7).
- Turner, I.L., Harley, M.D., Short, A.D., Simmons, J.A., Bracs, M.A., Phillips, M.S., Splinter, K.D., 2016. A multi-decade dataset of monthly beach profile surveys and inshore wave forcing at Narrabeen, Australia. *Sci. data* 3, 160024. <https://doi.org/10.1038/sdata.2016.24>.
- van der Walt, S., Schönberger, J.L., Nunez-Iglesias, J., Boulogne, F., Warner, J.D., Yager, N., Gouillart, E., Yu, T., 2014. scikit-image: image processing in Python. *PeerJ* 2, e453. <https://doi.org/10.7717/peerj.453>.
- VLIZ, 2018. sea level station monitoring facility [WWW Document]. Unesco/Ioc. <http://www.ioc-sealevelmonitoring.org/index.php>. accessed 5.14.19.
- Vos, K., 2019. Training data for: CoastSat image classification. Zenodo Digital Repository. <https://doi.org/10.5281/zenodo.3334147>.
- Vos, K., Harley, M.D., Splinter, K.D., Simmons, J.A., Turner, I.L., 2019. Sub-annual to multi-decadal shoreline variability from publicly available satellite imagery. *Coast. Eng.* 150, 160–174. <https://doi.org/10.1016/j.coastaleng.2019.04.004>.
- Xu, H., 2006. Modification of normalised difference water index (NDWI) to enhance open water features in remotely sensed imagery. *Int. J. Remote Sens.* 27, 3025–3033. <https://doi.org/10.1080/01431160600589179>.
- Young, I.R., Ribal, A., 2019. Multiplatform evaluation of global trends in wind speed and wave height. *Science* 80, 9527 eaav9527. <https://doi.org/10.1126/science.aav9527>.